https://doi.org/10.1088/1361-6463/ab3c7b

Parametric study of the radial plasma-wall interaction in a Hall thruster

A. Domínguez-Vázquez[1], F. Taccogna[2], P. Fajardo[1], E. Ahedo[1]

[1]Equipo de Propulsión Espacial y Plasmas, Universidad Carlos III de Madrid, Leganés, Spain, addoming@ing.uc3m.es

[2]Istituto per la Scienza e la Tecnologia dei Plasmi, CNR, via Amendola 122/D, 70126 Bari, Italy, francesco.taccogna@cnr.it.

Abstract

An investigation on the influence of relevant parameters on an annular Hall effect thruster plasma discharge is performed using a radial particle-in-cell simulation code with secondary electron emission from the walls and prescribed axial electric and radial magnetic fields. A simulation with true-secondary electrons only is taken as reference. First, the near-wall conductivity effects on the magnetized secondary electrons are illustrated by doubling the $\boldsymbol{E} \times \boldsymbol{B}$, allowing a further code validation. Second, when secondary backscattered electrons are included, the enhanced secondary emission yields lower sheath potential drops and primary electron temperature. Moreover, the dominant backscattered electrons increase the average secondary electrons emission energy, greatly affecting its temperature anisotropy ratio and increasing the replenishment level of the wall collectable tails of the primary electrons velocity distribution function. Third, the effect of the true-secondary electrons emission energy on the potential profile is shown to be negligible, the latter being mainly set by the dominant magnetic mirror effect. Finally, a planar case featuring symmetric plasma profiles permits to confirm the validity of the large cylindrical asymmetries present in the reference case, induced by the combined effects of the geometric expansion, the magnetic mirror and the centrifugal force (due to the $\boldsymbol{E} \times \boldsymbol{B}$ drift). A smaller deviation of the primary electron momentum equation from the Boltzmann relation along the magnetic lines is still found in the planar case, induced by the parallel temperature non-uniformity.

1 Introduction

Despite the fact that the Hall effect thruster (HET) [1–5] is already a mature technology successfully covering the propulsive needs of a wide variety of space missions,there exist relevant physical phenomena driving the HET plasma discharge which are not well understood yet. This hinters the development of reliable simulation tools that are essential for both heading optimized HET designs for new applications (e.g. very high or very low powers), and reducing development time and costs by predicting thruster lifetime and operational parameters at different regimes of interest (e.g. high thrust or high specific impulse scenarios).

One of these open problems is the interaction of the rarefied plasma discharge with the thruster walls. That interaction is responsible for plasma recombination, energy losses, and wall erosion.

Moreover, the low collisionality of the discharge prevents from reaching a full replenishment of the wall-collected high-energy tails of the electron velocity distribution function (VDF). This fact, along with the high secondary electron emission (SEE) caused by the 'primary' (or bulk) electron impact on the ceramic thruster walls enhances the departure of the electron VDF from a Maxwellian one.

Previous particle-in-cell (PIC)/Monte Carlo collision (MCC) formulations [6–8] of a one-dimensional planar (1Dp) scenario with a fixed neutral background determined the temperature anisotropy ratio of the electron VDF for several values of the axial electric field, collisional frequencies and SEE yields [9–11]. These results confirmed the partial recollection at the walls and partial thermalization within the plasma bulk of secondary electrons predicted by Ahedo and Parra [12]. and the near-wall conductivity (NWC) effect in the axial electron current proposed by Bugrova et al. [13].

In a recent paper [14], we presented a highly improved version of the 1D radial (1Dr) PIC/MCC model of an annular HET plasma discharge originally developed by Taccogna [15–17]. Assuming a radial divergence-free magnetic field and significant SEE from the lateral ceramic thruster walls, the cylindrical asymmetries in the discharge structure appear naturally. Improvements incorporated to the model have increased its numerical consistency and extend its capabilities. First, an ionization-controlled discharge algorithm assured a stationary discharge featuring a prescribed mean plasma density without the need of an axial particle contribution of plasma. Second, the secular growth of ion axial energy and the subsequent refreshing of ion macroparticles was avoided by canceling the ion axial acceleration, the new born ions being generated into the domain with a prescribed mean axial velocity instead. Finally, an extended volumetric weighting algorithm allowed to obtain much more reliable estimates of the relevant macroscopic magnitudes characterizing the low populated species, such as the secondary electrons.

Ref. [14] was focused on (i) defining and analyzing the improved numerical algorithms simulating the discharge and (ii) testing the code capabilities with a single simulation case. The present work affords, through several simulation cases, an investigation of the role of relevant model parameters in the plasma response, with the goals of further validate and benchmark the numerical model, and get a deeper insight into the physics of the discharge. In particular, it is aimed to analyze the effects on the discharge of: (1) changing electric and magnetic field strengths, (2) including elastically backscattered and rediffused electrons in the SEE yield, (3) emitting colder true-secondary electrons from the walls, and (4) using a planar channel. This last study will allow to corroborate the validity of the large asymmetries found in the radial plasma profiles for the annular case. The central role of the secondary electrons on the structure of the discharge motivates the exploration of the effects of non-true-secondary electrons on the SEE yields. The other two studies try to confirm the main physics of the discharge.

The paper is structured as follows. Sec. 2 outlines the main physical and numerical aspects of the

model, while the discussion of the results for each simulated scenario is provided in Sec. 3. Finally, the conclusions are presented in Sec. 4.

2 The radial model

The main aspects of the numerical model of Ref. [14] are summarized here. Fig. 1 sketches an annular HET chamber with r_1 and r_2 as inner and outer radius. The 1D radial (1Dr) model simulates a radial section located near the chamber exit within the acceleration region, where a significant axial electric field exists and ionization and wall recombination compensate approximately each other [18]. The 1Dr model considers electrons e, singly charged ions i, and neutrals n. Electrons and ions are modelled as two populations of macroparticles with densities and temperatures, n_j and T_j $(j = i, e)$, respectively. Every simulated macroparticle features the same macroparticle weight W, or number of elementary particles, which remains constant throughout the simulation. Neutrals are modeled just as a spatially uniform background with a constant temperature T_n and a time-dependent density $n_n(t)$, which is controlled to achieve a given average plasma density, as we explain next.

The PIC 1Dr model must fulfill the macroscopic conservation equations for ions and electrons

$$\frac{\partial n_j}{\partial t} + \frac{1}{r}\frac{\partial}{\partial r}(r n_j u_{rj}) = S_{ioniz} + S_{axial,j}, \qquad j = i, e, \tag{1}$$

where $n_j u_{rj}$ is the species radial flux, S_{ioniz} is the source term due to ionization, which is proportional to $n_n(t)$, and $S_{axial,j}$ is the source term due to the net axial contribution for species j. The term $S_{axial,j}$ contains information that is external to the radial model, and thus depends on the HET radial section to be simulated. In order to simulate a quasi-stationary discharge featuring a prescribed mean plasma density $\bar{n}_e(t) \approx \text{const} = n_{e0}$, the wall losses must be balanced out by the ionization and axial source terms. The ionization controlled discharge (ICD) algorithm presented in Ref. [14] assures a stationary discharge by setting $S_{axial,j} = 0$ (thus avoiding the need for an external axial plasma contribution), and adjusting $n_n(t)$ so that the wall losses are compensated by the ionization source term S_{ioniz}.

The divergent-free radial magnetic field satisfies

$$B_r(r) = B_{r1}\frac{r_1}{r}, \tag{2}$$

with B_{r1} known at r_1. The 1Dr model prescribes also constant axial electric field E_z. This field, combined with the radial magnetic field, forces the electron $\boldsymbol{E} \times \boldsymbol{B}$ azimuthal drift. However, in order to avoid ion particle refreshing, the model avoids secular axial acceleration of ions by E_z. Instead, ion macroparticles are inserted initially or created later (through the ionization of the neutral gas) with a mean axial velocity u_{zi}.

On the contrary, both ions and electrons are influenced by the radial electric field, $E_r = -d\phi/dr$, with $\phi(r,t)$ the electric potential, which is self-consistently obtained from

$$\frac{\varepsilon_0}{r}\frac{\partial}{\partial r}\left(r\frac{\partial \phi}{\partial r}\right) = \rho_{el}(r,t), \tag{3}$$

with ρ_{el} standing for the net electric charge density of the plasma, and the boundary conditions

$$\phi_2 = 0, \qquad \varepsilon_0 E_{r2} = -\sigma_2(t), \tag{4}$$

at the outer wall, $r = r_2$, where ε_0 is the vacuum permittivity and σ_2 is the surface charge density there. It can then be shown that $\varepsilon_0 E_{r1} = \sigma_1(t)$, with σ_1 the surface charge at $r = r_1$, is satisfied automatically [14]. The above surface charge densities originate from the charge accumulation at the thruster walls, and are obtained by integrating over time the net electric current density collected at the walls

$$\sigma_l(t) = -\int dt \boldsymbol{j}_l(t)\cdot \mathbf{1}_l, \quad l = 1,2, \tag{5}$$

where $\boldsymbol{j}_l$ is the net electric current density to the wall and $\mathbf{1}_l$ is the wall normal versor pointing towards the plasma.

Second-order finite-difference schemes are used for discretizing Poisson equation along the cylindrical radial coordinate r. Once the radial electric field is updated, macroparticles are propagated along time using the Boris-Buneman leapfrog algorithm [6]. The timestep is chosen so that $\Delta t < 0.3\omega_{pe}^{-1}$, where ω_{pe} is the plasma frequency. This condition ensures an accurate integration of the electron gyromotion since $\omega_{pe} > \omega_{ce}$, with ω_{ce} the electron gyrofrequency (see Tab. 1).

Plasma macroscopic properties are computed at the mesh nodes through the area weighting algorithm of Ref. [6] and including the corrected nodal weighting volumes (for canceling cylindrical effects) of Ref. [19]. The extended volumetric weighting (EVW) algorithm presented in Ref. [14], which, by taking into consideration data from a number of simulation timesteps yields much more accurate estimates of the macroscopic properties of the low populated species (such as the secondary electrons) while not affecting those of the dominant species (i.e. primary electrons and ions), is used.

Regarding plasma-wall interaction, ions and electron reaching the radial walls are collected and thus eliminated from the simulation domain. Ion recombination is not explicitly simulated however, although the adjusting of the neutral background density $n_n(t)$ performed by the ICD algorithm ultimately represents this phenomenon. The total SEE yield produced by the impacting electrons follows the probabilistic model of Ref. [20], which includes the emission of elastically backscattered, rediffused and true-secondary electrons. The corresponding yields and the energy distribution function of the secondary electrons are depicted in Fig. 3 of Ref. [16] for different impacting electron energies,

and not reproduced here. In the following, we shall distinguish between the true-secondary (TS) electrons, which feature a semi-Maxwellian emission from the walls with average emission energy T_{eW}, and the non-true-secondary (NTS) electrons, gathering both the backscattered and rediffused ones, for which the emission energy depends on the impacting electron (see Ref. [20]).

The treatment of collisions between different populations and the applied MCC algorithms can be found in [14]. Secondary electrons are transferred to the primary population when they undergo a collision with neutrals or a large angle (higher than 90 degrees) Coulomb collision. For the sake of facilitating the analysis of the plasma discharge response, three different electron species are considered hereafter: primary electrons p, and secondary electrons emitted by the inner $s1$, and outer $s2$ walls. An electron turbulent collisionality, included in previous works [9–11], has not been considered here: it should be relevant only for the $\boldsymbol{B}$-perpendicular (i.e. axial) electron transport and thus we preferred not adding an extra phenomenological parameter.

3 Results

Considering xenon as propellant, Tab. 1 lists the main model input parameters for the reference case of Ref. [14], Case 1 here, and gathers the changes from that case, defining the rest of Cases 2 to 5 studied in the present work:

- Case 2 analyzes the effect of doubling the electric and magnetic fields responsible of the Hall effect.
- Case 3 discusses the effect of including backscattered secondary electrons.
- Case 4 investigates the effect of a colder emission of true-secondary electrons.
- Case 5 analyzes the discharge in a planar discharge channel.

The analysis of the stationary plasma discharge obtained for the cylindrical Cases 1-4 and the planar Case 5 are presented in Secs. 3.1 and 3.2, respectively. For all cases, the macroparticle weight W is selected so that the initial number of both electron and ion macroparticles is $N_{p0} \approx 10^5$, corresponding to about 70 macroparticles per cell. It has been checked that using double the number of particles per cell reduces only the PIC fluctuations, without changing the average trends. The simulations are started assuming uniform Maxwellian populations of electrons and ions of the same density. In the first timesteps, this implies large electron currents to the walls. These build up negative surface charges there, which within 1 μs create the Debye sheaths that confine electrons. The surface charges reach a steady state when the net electric currents to the walls become zero [see Eq. (5)].

Figures 2 to 4 show the radial profiles of the main plasma macroscopic magnitudes obtained through the EVW algorithm at near stationary conditions. Those include particle densities, temperatures and

drift velocities for the different electron populations. The electric potential profiles are depicted in Fig. 2(a). For the sake of clarity, the offset (of 1000 m) in the radial coordinate for Case 5 is eliminated for plotting purposes. For all cases, points W_1, W_2, and M, indicated in Figs. 1 and 2(a), correspond to the inner and outer walls, and to the channel mid radius, respectively. The vertical dashed lines in Figs. 2-4, located at 0.5 mm ($\sim 6\lambda_D$) from the walls, represent approximately the inner and outer edges of the Debye sheaths (points Q_1 and Q_2), where the radial ion Mach number is found to be approximately 1 and the profiles slopes change sharply. The definition of *sheath edges* in the present one-scale model is just meant for remarking differences between the plasma responses at the plasma bulk and near the thruster walls. The discussion here is focused on the plasma bulk profiles. Additionally, Fig. 5 shows the p and $s2$ electron VDFs at the points M, Q_1 and Q_2 for cases 1, 3 and 5, respectively, and Tab. 2 summarizes the relevant data of the 5 discharges, including the electric potentials at the aforementioned points, the electron current densities collected at the walls, the mean wall impact energies (per elementary particle), the SEE yields, the secondary electrons wall collection and p-electron conversion fractions, and the electron temperature values at M.

3.1 Cylindrical discharges

Case 2 is meant mainly to check the reliability of the numerical code in reproducing the electron dynamics. By doubling the axial electric field and the radial magnetic field, first the azimuthal drift velocity $u_\theta = (\boldsymbol{E} \times \boldsymbol{B})/B^2 = E_z/B_r$ remains the same, which is confirmed in Fig. 2(g) for the primary electrons, and in Figs. 4(c) and 4(d) for the secondary electrons, respectively. On the other hand, the gyroradius of the electrons is halved and the corresponding gyrofrequency is doubled. As a consequence, the wall-emitted secondary electrons perform double the number of gyroorbits in one inter-wall journey. This is confirmed by the double number of peaks (with respect to Case 1) in the azimuthal and axial macroscopic velocity profiles of wall-emitted secondary electrons, shown in Figs. 4(c) and 4(e) for the $s1$-electrons, and in Figs. 4(d) and 4(f) for the $s2$-electrons, respectively. The well known near wall conductivity (NWC) phenomenon [13] is responsible for the oscillations present in the secondary electrons drift velocities above. As for the primary electrons, Fig. 2(h) shows that the axial drift velocity profile is close to zero. Since there are not secular effects on the axial flow of any of the populations, the simulations confirm that there is no need of performing axial particle refreshing.

The rest of plasma profiles of Case 2 characterizing the stationary discharge remain the same (see the electric potential profile in Fig. 2(a), and the density, temperature and drift velocity profiles depicted in Figs. 2(b)-(h) for the p-electrons, and in Figs. 3 and 4 for both the $s1$ and $s2$ electrons). The higher PIC-related noise level affecting the statistics of the least populated $s1$-electrons explains the larger discrepancies found in their density and temperature profiles. The same applies to the relevant

discharge data shown in Tab. 2. The physical reasons behind this fact are the following. Given the same initial populations, the cycloidal motion described by every (primary) electron macroparticle in Case 2 features the same drift and thermal energy than in Case 1. As a consequence, (*i*) the balance between the wall losses and the ionization collisions stated in Eq. (1) leads to the same primary electron density profile, which in turn shapes the same electric potential radial profile, according to Eq. (3); (*ii*) the primary electrons radial and perpendicular temperature profiles respond to the same velocity dispersion level both in the direction parallel to the magnetic field and in the $\boldsymbol{B}$-perpendicular plane, respectively; (*iii*) the wall-collected primary electrons produce the same SEE from the ceramic walls; and (*iv*) the density and temperature profiles yield the same low collisional regime, in which Coulomb collisions are negligible compared to electron-neutral collisions. In all cases, the dominant elastic *e*-*n* collision frequency is ∼3.7 MHz, being still low compared to the radial transit frequency, ∼62 MHz. In the remainder of this Section, the main aspects of the discharge are discussed taking Case 1 as reference for the comparison with Cases 3 and 4.

The electric potential radial profiles are depicted in Fig. 2(a). The corresponding values at the points W_1, W_2, Q_1, Q_2, and M are listed in Tab. 2. As already found in Ref. [14] for Case 1, the magnetic mirror effect and the centrifugal force in the cylindrical geometry lead to asymmetric radial profiles of the different plasma macroscopic magnitudes of both the primary and secondary electrons. Neglecting collisions and invoking the electron total energy conservation in the small electron Larmor radius limit, the net radial (i.e. $\boldsymbol{B}$-parallel) energy change for an electron moving inwards from the outer wall may be written as

$$\frac{m_e}{2}(v_r^2(r) - v_{r,W_2}^2) = e\phi(r) - \mu B_{r1}\left(\frac{r_1}{r} - \frac{r_1}{r_2}\right) - W_{d1}\left(\frac{r^2}{r_1^2} - \frac{r_2^2}{r_1^2}\right), \tag{6}$$

where the radially varying magnetic field, Eq. (2), induces two effects: first, the second term of the right side assesses the change in the $\boldsymbol{B}$-perpendicular electron energy associated to the electron gyromotion due to the magnetic mirror effect, which is proportional to the conserved magnetic moment μ; second, the third term of the right side represents the radial change in the electron $\boldsymbol{E}\times\boldsymbol{B}$ drift energy, $W_{d1} = m_e E_z^2/2B_{r1}^2$ being the gyrocenter azimuthal energy at the inner wall. For both Cases 1 and 2, $W_{d1} = 1.27$ eV and $W_{d2} = 2.58$ eV at the inner and outer walls, respectively. On the other hand, the average energy associated to the velocity dispersion in the $\boldsymbol{B}$-perpendicular plane is $\langle\mu B\rangle = 7.5$ eV. Given the low collisional regime, this energy is mostly due to the gyromotion and coincides with the average $\boldsymbol{B}$-perpendicular electron temperature in the plasma bulk, thus further validating the simulation results. According to Eq. (6), the potential drop between the two walls, $\Delta\phi_{W_1W_2} > 0$, and the decrease on the $\boldsymbol{E}\times\boldsymbol{B}$ drift energy from W_2 to W_1 facilitate the collection at the wall W_1 of electrons emitted from the wall W_2. On the contrary, the magnetic mirror effect opposes the electron

collection at W_1.

Fig. 5 shows the radial VDF (once integrated over the azimuthal and axial velocities) for the p and $s2$-electrons at the points M, Q_1 and Q_2 (the results for the $s1$-electrons are analogous to those of the $s2$ electrons and have been omitted). The black and green lines with circle and up-triangle markers refer to Case 1 and Case 3, respectively. The vertical lines of corresponding colors separate the regions containing radially confined electrons from those left and right regions with electrons to be collected at the inner and outer walls, respectively. Cases 2 and 4 show a similar behavior and have been omitted for the sake of clarity. The results reveal a dominant primary electron density in the plasma bulk (i.e. between Q_1 and Q_2) with respect to that of the secondary electrons, which is consistent with the density profiles shown in Figs. 2(b), 3(a) and 3(b) for p, $s1$ and $s2$-electrons, respectively, confirming the much lower density of the secondary electrons and thus their minor role in shaping the electric potential.

The VDFs present a large high-energy tails depletion, only partially refilled with wall-collectable electrons by the infrequent collisions. The peaks in the $s2$-VDFs at Q_2, shown in Fig. 5(f), correspond to the radial energy gain through the sheath of the $s2$-electrons emitted from W_2, which, neglecting magnetic effects and collisions within the thin sheath, is approximately equal to the corresponding sheath potential fall. For Case 1, the latter are $\Delta\phi_{Q_1W_1} = 11.68$ V and $\Delta\phi_{Q_2W_2} = 12.86$ V at the inner and outer walls, respectively. The larger secondary emission found in Case 3, commented below, decreases the sheath potential falls by a value of $\sim$0.5 V and of $\sim$1.5 V with respect to Case 1 at the inner and outer walls, respectively, yielding $\Delta\phi_{Q_1W_1} = 11.18$ V and $\Delta\phi_{Q_2W_2} = 11.36$ V [see Fig. 2(a) and the electric potential values at Tab. 2]. The wall recollection and the conversion into primary electrons through the collisions (electron-neutral and large angle Coulomb collisions) shape the secondary electron VDFs along the domain, thus determining the density and other macroscopic properties of the secondary electrons. According to Figs. 3(a) and 3(b), in Case 3 the secondary electrons feature a density around one order of magnitude higher than in Case 1. This is also evident from the inspection of the $s2$-VDFs depicted in Figs. 5(b), 5(d) and 5(f).

Tab. 2 reveals a large asymmetry in the electron currents collected at the inner and outer walls. Except for Case 3, commented below, most of these currents come from the much more populated p-electrons. Since the two wall materials are the same, the different values of the average electron impact energy (per elementary particle) shown in Tab. 2, computed as the ratio between the net energy flux deposited to the wall and the corresponding particle flux, explain the different SEE yields obtained at the inner and outer walls. For instance, at the wall W_1, the average total secondary emission yield of $s1$-electrons, $\delta_{SEE,1}$, is computed as the sum of the average yields corresponding to

the TS and NTS electrons, given by

$$\delta_{TS,1} = \frac{|j_{TS,s1,1+}|}{|j_{e,1-}|}, \quad \delta_{NTS,1} = \frac{|j_{NTS,s1,1+}|}{|j_{e,1-}|}, \tag{7}$$

respectively, where $j_{e,1-}$ is the total electron current density collected at W_1, and $j_{TS,s1,1+}$ and $j_{NTS,s1,1+}$ are the TS and NTS current densities of $s1$-electrons emitted from the wall W_1, respectively. In particular, for Case 1 featuring true-secondary electron emission only, values of $\delta_{SEE,1} = 0.16$ and $\delta_{SEE,2} = 0.28$ are obtained at the inner and outer walls, respectively. In contrast, Case 3 features considerably larger total SEE yields: $\delta_{SEE,1} = 0.81$ and $\delta_{SEE,2} = 0.83$ at the inner and outer walls, respectively, with dominant emission of NTS electrons (see how $\delta_{NTS} > \delta_{TS}$ in Tab. 2). Considering the average electron wall-impact energies listed in Tab. 2, these results are consistent with the SEE analysis presented in Ref. [16]. It is worth pointing out that the space charge saturation regime, estimated at $\delta \approx 0.98$, is not achieved in our simulations for the prescribed value of the axial electric field.

In Case 1, the sheath potential falls are around 6 times higher than the average secondary emission energy T_{eW}. However, the emission energy for the backscattered electrons depends on the energy of the impacting primary (and secondary) electrons to the walls, thus leading to a larger coupling between the dynamics of the impacting and emitted electrons. In Case 3, the dominant emission of NTS electrons increases the average wall emission energy to ∼7.85 eV and ∼8.53 eV at the inner and outer walls, respectively. These values are thus much closer to the aforementioned lower sheath potential falls for this case [see the potential values in Tab. 2 and the potential profiles in Fig. 2(a)]. As a result, significantly larger electron currents are collected to the walls, the inner wall collecting a larger current of $s2$-electrons than of p-electrons (see Tab. 2), as confirmed by the more populated $s2$-VDF inner wall collectable tails shown in Figs. 5(b), 5(d) and 5(f), with respect to those of the p-electrons depicted in Figs. 5(a), 5(c) and 5(e).

Tab. 2 also provides the fractions of secondary electrons recollected at each wall and transferred to the primary population through collisional processes. For Case 1, the p-conversion/recollection proportion of both the $s1$ and the $s2$-electrons is around 60%-40% and 50%-50% for the $s1$ and the $s2$ electrons, respectively, while for Case 3 the proportions are around 25%-75% and 35%-65% for the $s1$ and the $s2$ electrons, respectively. Since the collisional frequencies remain approximately the same as in Case 1, this fact confirms a net increase in the secondary electron wall recollection.

The replenishment via collisions of the high energy tails of the p-electrons VDF was modeled by Ahedo and de Pablo [21] through the replenishment parameter σ_t (not to be mistaken for the surface

charge), which, for instance, at the inner wall W_1 is defined as

$$\sigma_{t,1} = \frac{|j_{p,1-}|}{j_{ther,1}}, \quad \text{with} \quad j_{ther,1} = e n_{pQ_1} \exp\left(-\frac{e\Delta\phi_{Q_1W_1}}{T_{pQ_1}}\right)\sqrt{\frac{T_{pQ_1}}{2\pi m_e}}, \tag{8}$$

where n_{pQ_1} and T_{pQ_1} are the primary electrons particle density and total temperature at Q_1, respectively. Tab. 2 lists the values of σ_t at each wall. Interestingly, the replenishment ratio depends on the secondary electron emission, Case 3 featuring values about 2 times higher with respect to Case 1. Given the aforementioned higher average emission energy of the secondary electrons in Case 3, the secondary electron population features a larger average energy with respect to that in Case 1. Thus, the secondary electrons transferred to the primary electron population via collisions yield a higher replenishment of the high energy tails of the p-VDF, as it is confirmed by the more populated wall-collectable tails of the p-VDF shown in Fig. 5(a) for Case 3, with respect to that of Case 1.

The macroscopic radial velocity profiles for the p, $s1$ and $s2$ electron populations are depicted in Figs. 2(f), 4(a) and 4(b), respectively. Primary electrons behave as usual with fluxes from the channel mid-point M to the walls. The velocity increase inside the sheaths is just the consequence of the decreasing density there. The $s1$-electrons present a net outwards radial velocity, indicating that their outwards flow is slightly larger than the inwards one, due to a larger recollection at W_2. This situation is particularly evident in Case 3, in which the $s1$ recollection at the inner wall only amounts up to a 3% (see Tab. 2). The $s2$-electrons exhibit the opposite behavior. Notice that in all cases these radial velocities represents just small drifts of the VDFs of the three electron populations. Even the largest value of $u_r \approx 3.5 \cdot 10^5$ ms^{-1} for the $s1$-electrons in Case 3 at $Q1$ corresponds to an energy of only $\sim$0.35 eV.

Figs. 2(c)-(e) show, respectively, the profiles of the radial (i.e. $\boldsymbol{B}$-parallel) and the $\boldsymbol{B}$-perpendicular temperature, and the ratio $T_r/T_\perp$ for the p-electrons. On the other hand, Figs. 3(c), 3(e) and 3(g), and Figs. 3(d), 3(f) and 3(h) show the radial profiles of T_r, $T_\perp$ and $T_r/T_\perp$ for the $s1$ and $s2$ electrons, respectively. In all cases, $T_\theta \approx T_z \approx T_\perp$. The temperature values at the point M are listed in Tab. 2 for all the electron species. The larger secondary emission in Case 3 yields lower primary electron temperatures with respect to Case 1. This fact is also evident from the higher (negative) slope of the radial p-VDF shown in Fig. 5(a), and it is consistent with the larger depletion of its high energy tails, favoured by the aforementioned lower sheath potential falls found in Case 3.

The temperature anisotropy, which is the combined consequence of the electron magnetization and depletion at walls, is different for the primary and secondary electrons [14]. Regarding the former, starting from an isotropic initial population with T_{e0}, the walls collect magnetized high-energy p-electrons along the radial direction (i.e. normal to the walls). Since the low collisionality regime prevents the fully replenishment of the radial p-VDF wall-collected high energy tails, the p-electrons

presents a temperature anisotropy ratio $T_r/T_\perp < 1$ at stationary conditions, the radial temperature profile responding to the radial velocity dispersion due mainly to the bouncing between the sheaths, while the $\boldsymbol{B}$-perpendicular temperature is dominated by the velocity dispersion associated to the electron gyromotion.

In contrast, let us consider a true-secondary electron emitted, for instance, from the outer wall with a total energy T_{eW}. After crossing the outer wall sheath, it describes a cycloidal motion in the plasma bulk towards the inner wall characterized by a radial (i.e. $\boldsymbol{B}$-parallel) energy of the order of the radial energy gain through the sheath, i.e. $e\Delta\phi_{Q2W2} \gg T_{eW}$, and a gyroenergy of the order of T_{eW}. This electron may perform several inter-wall journeys before being recollected at the walls or transferred to the primary population via collisions. As a consequence, secondary electrons act like two opposite beams, the dominant electron-neutral and the large angle Coulomb collisions not contributing to any velocity dispersion, its radial bouncing being thus the major responsible for its radial and $\boldsymbol{B}$-perpendicular temperatures. The aforementioned larger net energy contained in the radial direction, compared to that in the $\boldsymbol{B}$-perpendicular plane, explains the temperature anisotropy ratio $T_r/T_\perp > 1$ for secondary electrons. Interestingly, as shown in Fig. 3(h), the $s2$-electrons temperature anisotropy ratio is closer to one for Case 3. This fact is mainly induced by the dominant backscattered $s2$-electrons, which, as aforementioned, feature a wall-emission energy of the order of the sheath potential falls, thus increasing the average $\boldsymbol{B}$-perpendicular energy of the secondary electrons and contributing to the higher $T_\perp$ profile shown in Fig. 3(f).

On the other hand, in Case 4 the true-secondary electrons are emitted with 10 times less energy (i.e. T_{eW} is ten times lower) with respect to Case 1. As expected, the secondary electrons exhibit lower $\boldsymbol{B}$-perpendicular temperature profiles [see Figs. 3(e) and 3(f)]. Interestingly, the potential difference between the two walls, $\Delta\phi_{W_1W_2}$, is not significantly affected by T_{eW} and remains close to that of Case 1, being thus mainly set by the dominant magnetic mirror effect. The same applies to the sheath potential falls at the two walls. Therefore, according to its lower wall-emission energy, they spend a longer time bouncing radially between the sheaths, where an eventual collision may transfer them to the primary population. This explains (*i*) the significantly larger p-conversion fractions of both the $s1$ and $s2$ electrons in this case (see Tab. 2), and (*ii*) the lower absolute values of the macroscopic radial velocity profiles of secondary electrons [see Figs. 4(a) and 4(b)]. However, contrary to Case 1, which features similar wall impact energies of secondary electrons at the corresponding opposite walls (i.e. $E_{ws1,2} \sim E_{ws2,1}$) when $T_{eW} \sim \Delta\phi_{W_1W_2}$, the fact that $T_{eW} \ll \Delta\phi_{W_1W_2}$ leads to $E_{ws2,1} - E_{ws1,2} \sim \Delta\phi_{W_1W_2}$ in Case 4. Nevertheless, the impact energy of the dominant p-electrons, and thus the secondary emission yields, remains approximately the same. The influence of the wall temperature in the rest of plasma radial profiles is negligible.

3.2 Planar discharge

The simulation domain is artificially displaced 1000 m towards larger radii in order to simulate the planar scenario of Case 5, in which the geometric cylindrical expansion effects (i.e. terms $\sim$1/r) must vanish. According to Eq. (2), $B_{r2}/B_{r1} = r_1/r_2 = 0.99985 \simeq 1$, so that the applied radial magnetic field is approximately constant along the radial domain. The value B_{r1} is set to the average magnetic field value between the two walls (see Tab. 1), while the rest of simulation parameters are kept equal to those of Case 1.

As shown in Figs. 2(g), 4(c) and 4(d) for the p, $s1$ and $s2$ electrons, the $\boldsymbol{E}\times\boldsymbol{B}$ drift is approximately constant along the radial domain, so that the third term in the right hand side of Eq. (6) naturally cancels out. Likewise, the magnetic mirror effect becomes negligible along the simulation domain. As a result, the asymmetries in the radial profiles and in the different magnitudes at the walls for all the electron populations vanish (see Figs. 2-4 and the relevant discharge data in Tab. 2). The symmetry of the p-electrons VDF at the point M shown in Fig. 5(a) is also evident. According to the radial profiles of the ratio $T_r/T_\perp$ shown in Figs. 2(e), 3(g) and 3(h), the temperature anisotropy of the different electron populations exhibit the same trend as in the cylindrical cases.

Neglecting collisions, the macroscopic radial equilibrium for p electrons integrated along the radial coordinate yields [14]

$$e\phi - e\phi_M - T_{rpM}\ln\frac{n_p}{n_{pM}} = \left[T_{rp} - T_{rpM} + \int_{r_M}^{r} dr\,(T_{rp} - T_{rpM})\,\frac{d\ln n_p}{dr}\right] + \\ + \int_{r_M}^{r} dr\frac{T_{rp} - T_{\perp p}}{r} - \int_{r_M}^{r} dr\frac{m_e u_{\theta p}^2}{r}. \tag{9}$$

The left side of Eq. (9) groups the terms of the Boltzmann relation while the right side contains the following three terms: (i) the non-uniform radial temperature contribution, (ii) the magnetic mirror effect, which in turn is a combination of temperature anisotropy and cylindrical expansion, and (iii) the centrifugal force. The results shown in Ref. [14] for Case 1 are here compared to those of Case 5 in Fig. (6). The whole radial equilibrium of Eq. (9) is excellently satisfied in both cases confirming the marginal role of the collisional processes and other convection effects. In Case 1, the three terms of the right side of Eq. (9) are of the same order and the sum of these contributions introduces a correction of up to 30% (relative to $e\phi - e\phi_M$) in the Boltzmann relation [14]. In Case 5 however, the cylindrical terms corresponding to the magnetic mirror effect and the centrifugal force (i.e. terms $\sim 1/r$) vanish, so that the correction below reduces approximately up to 15% and is mostly due to the non-uniform radial temperature profile, a contribution generally neglected.

Finally, the comparison of the resulting plasma magnitudes at W_1 and W_2 in the symmetric planar Case 5 allows a rough estimation of the PIC-related noise induced error of about 1% in our simulations.

4 Conclusions

This work has further advanced in the analysis of effects of the interaction with the radial, dielectric walls of a Hall effect thruster on the electron VDF and the resulting plasma discharge structure. Five simulation cases have constituted the investigation of the plasma response when central parameters of the model are varied. These simulations have allowed, on the one hand, to reinforce the confidence on the numerical algorithms first presented in Ref. [14] and, on the other hand, to get deeper insight into the physical phenomena.

The comparison of the reference Case 1 and Case 2, where both the radial magnetic field and the axial magnetic field are doubled, has been important in two ways: first, to illustrate the magnetization of secondary electrons (just after their emission) and the relation of near-wall conductivity to the electron gyroorbit; second, to validate the numerical algorithms by keeping without change the rest of the macroscopic behavior.

Case 3 explores the influence of the secondary backscattered electrons, which were omitted in Case 1. SEE yield data from Ref. [20] provides a predominance of backscattered electrons for the range of electron energies here. This implies an increase of the average emission energy of the secondary electrons and greatly modifies the radial structure of the discharge. The enhanced SEE reduces the sheath potential drops facilitating the electron wall collection. This could explain the decrease of the p-population temperature in the bulk plasma. In addition, it changes the anisotropy ratio $T_r/T_\perp$ of secondary electrons. Moreover, the conversion to primary electrons of these backscattered electrons via collisions yields a higher replenishment of the wall-collectable tails of the primary electrons VDF.

Case 4 analyzes the influence of the true-secondary average electron emission energy T_{eW} on the plasma discharge, mainly in (i) the potential difference between inner and outer walls and (ii) the recollection fraction of secondary electrons. The effect of T_{eW} on the potential asymmetry is negligible, implying that this one is due to the dominant magnetic mirror effect. The effect on SEE recollection is mild.

Finally, Case 5 considers the plasma discharge in a planar chamber and has allowed to confirm the physical soundness of the large cylindrical asymmetries found in the original Case 1 of Ref. [14]. It is shown that all asymmetries disappear in Case 5. Furthermore, the comparison between results at inner and outer walls indicate that the numerical errors due to the PIC-related noise are in the range of a 1%, a very good value for a PIC code. This case also confirms that temperature anisotropy and radial non-uniformity are inherent to the rarefied plasma and the interaction with the wall in the presence of the applied magnetic field.

Work in progress is trying, first, to simulate plasma discharges with a higher axial electric field, when the SEE yield is near one, charge saturation effects at the wall can appear, and instabilities there can develop. Preliminary analyses show that the ICD algorithm can be inadequate for that

regime due to the larger relevance of secondary electrons. In the radial model, a higher E_z turns into an increase in the primary electron population energy, which consequently increases the SEE yields. Therefore, a situation may arise in which the electron production is dominated by the SEE, instead of by ionization of the neutral gas background. Second, simulations with a non-purely radial magnetic field seems to indicate substantial changes in the plasma discharge which need to be properly assessed yet.

5 Acknowledgments

The UC3M researchers have been supported by the PROMETEO-CM project, funded by the Comunidad de Madrid, under Grant Y2018/NMT-4750. Additional funding for A. Domínguez-Vázquez came from the Spain's National Research and Development Plan (Project ESP2016-75887). F. Taccogna has been supported by the italian Ministero dell'Istruzione, dell'Università e della Ricerca (MIUR) under the CLOSE project (grant ARS01_00141).

References

[1] E. Ahedo. Plasmas for space propulsion. *Plasma Phys. Control. Fusion*, 53(12):124037, 2011.

[2] D. M. Goebel and I. Katz. *Fundamentals of electric propulsion: Ion and Hall thrusters*. Willey, New York, 2008.

[3] R. G. Jahn. *Physics of electric propulsion*. McGraw-Hill, New York, 1968. (reprinted by Dover).

[4] M. Martínez-Sánchez and J. E. Pollard. Spacecraft electric propulsion-an overview. *Journal of propulsion and power*, 14(5):688–699, 1998.

[5] J. P. Boeuf. Tutorial: physics and modeling of Hall thrusters. *J. Appl. Phys.*, 121(1):011101, 2017.

[6] C. K. Birdsall and A. B. Langdon. *Plasma physics via computer simulation*. Adam Hilger, Bristol, Philadelphia and New York, 1991.

[7] C. K. Birdsall. Particle-in-Cell charged particle simulations, plus Monte Carlo collisions with neutral atoms, PIC-MCC. *Trans. Plasma Sci.*, 19(2):65–85, 1991.

[8] R. W. Hockney and J. W. Eastwood. *Computer simulations using particles*. Adam Hilger, Bristol and New York, 1988.

[9] D. Sydorenko, A. Smolyakov, I. Kaganovich, and Y. Raitses. Kinetic simulation of secondary electron emission effects in Hall thrusters. *Physics of Plasmas*, 13(1):014501, 2006.

[10] D. Sydorenko, A. Smolyakov, I. Kaganovich, and Y. Raitses. Modification of electron velocity distribution in bounded plasmas by secondary electron emission. *Plasma Science, IEEE Transactions on*, 34(3):815–824, 2006.

[11] I. D. Kaganovich, Y. Raitses, D. Sydorenko, and A. Smolyakov. Kinetic effects in a Hall thruster discharge. *Physics of Plasmas*, 14(5):057104, 2007.

[12] E. Ahedo and F. I. Parra. Partial trapping of secondary electron emission in a Hall thruster plasma. *Physics of Plasmas*, 12(7):073503, 2005.

[13] A.I. Bugrova, A. I. Morozov, and V. K. Kharchevnikov. Experimental studies of near wall conductivity. *Fizika Plazmy*, 16(12):1469–1481, 1990.

[14] A. Domínguez-Vázquez, F. Taccogna, and E. Ahedo. Particle modeling of radial electron dynamics in a controlled discharge on a Hall thruster. *Plasma Sources Science and Technology*, 27(6):064006, 2018.

[15] F. Taccogna, S. Longo, M. Capitelli, and R. Schneider. Particle-in-cell simulation of stationary plasma thruster. *Contributions to Plasma Physics*, 47(8-9):635–656, 2007.

[16] F. Taccogna, S. Longo, M. Capitelli, and R. Schneider. Surface-driven asymmetry and instability in the acceleration region of a Hall thruster. *Contrib. Plasma Phys.*, 48(4):1–12, 2008.

[17] F. Taccogna, R. Schneider, S. Longo, and M. Capitelli. Kinetic simulations of a plasma thruster. *Plasma Sources Sci. Technol.*, 17(2):024003, 2008.

[18] E. Ahedo, J. M. Gallardo, and M. Martínez-Sánchez. Effects of the radial-plasma wall interaction on the axial Hall thruster discharge. *Physics of Plasmas*, 10(8):3397–3409, 2003.

[19] J. P. Verboncoeur. Symmetric spline weighting for charge and current density in particle simulation. *Journal of Computational Physics*, 174:421–427, 2001.

[20] M. A. Furman and M. T. F. Pivi. Probabilistic model for the simulation of secondary electron emission. *Phys. Rev ST Accel. Beams*, 5(12):124404, 2002.

[21] E. Ahedo and V. de Pablo. Combined effects of electron partial thermalization and secondary emission in Hall thruster discharges. *Physics of Plasmas*, 14:083501, 2007.

Type	Description, symbol and units	Case 1	Changes from case 1
Populations settings	Number of elementary particles per macroparticle, W (-)	$3 \cdot 10^9$	Case 5: $7.06 \cdot 10^{13}$
	Initial average plasma density, n_{e0} ($10^{17}\mathrm{m}^{-3}$)	0.8	-
	Initial number of ions and electrons*, N_{p0} (-)	106814	-
	Initial electron temperature, T_{e0} (eV)	10	-
	Initial ion temperature, T_{i0} (eV)	1	-
	Ion axial mean velocity, u_{zi} (km/s)	10	-
	Initial background neutral density, n_{n0} (10^{17} m^{-3})	40	-
	Neutral temperature, T_n (K)	700	-
E, B fields	Electric field axial component, E_z (V/cm)	100	Case 2: 200
	Magnetic field radial component at inner radius, B_{r_1} (G)	150	Case 2: 300; Case 5: 124.84
Simulation parameters	Non-true-secondary emission	OFF	Case 3: ON
	True-secondary emission	ON	-
	Average true-secondary electrons emission energy, T_{eW} (eV)	2	Case 4: 0.2
	Inner radius, r_1 (cm)	3.5	Case 5: $10^5 + 3.5$
	Outer radius, r_2 (cm)	5.0	Case 5: $10^5 + 5.0$
	Number of nodes, N_r (-)	1500	-
	Grid spacing*, Δr (μm)	10	-
	Timestep, Δt, (ps)	5	-
Physical parameters	Debye length*, λ_D (μm)	83.1	-
	Electron Larmor radius*, r_l (μm)	802.0	Case 2: 401.0; Case 5: 963.7
	Inverse of plasma frequency*, $1/\omega_{pe}$ (ps)	62.7	-
	Inverse of electron cyclotron frequency*, $1/\omega_{ce}$, (ps)	379.1	Case 2: 189.5; Case 5: 455.5

Table 1: Main input parameters including initial population settings, externally applied fields and grid definition for Case 1 (reference case of Ref. [14]). The changes with respect to Case 1 defining the rest of cases considered are indicated in the last column. The magnitudes marked with an asterisk (*) are not input parameters of the model, but are derived from the other parameters instead. The variables named as physical parameters are estimated from the other input values given at initial conditions.

Type and units	Description and symbol	Case 1	Case 2	Case 3	Case 4	Case 5
Electric potentials (V)	At the mid radius M, ϕ_M	17.69	17.24	16.09	17.34	14.48
	At the inner sheath edge Q_1, ϕ_{Q_1}	13.90	13.45	12.21	13.59	10.22
	At the outer sheath edge Q_2, ϕ_{Q_2}	12.86	12.50	11.36	12.64	10.14
	At the inner wall W_1, ϕ_{W_1}	2.22	2.21	1.03	2.31	−0.05
	At the outer wall W_2, ϕ_{W_2}	0.00	0.00	0.00	0.00	0.00
Current densities (A/m^2)	p to the inner wall, $\lvert j_{p,1-}\rvert$	12.21	12.35	17.32	13.32	18.45
	$s1$ to the inner wall, $\lvert j_{s1,1-}\rvert$	0.18	0.23	1.66	0.23	0.22
	$s1$ from the inner wall, $\lvert j_{s1,1+}\rvert$	2.50	2.66	56.55	2.41	4.30
	$s2$ to the inner wall, $\lvert j_{s2,1-}\rvert$	3.57	3.52	51.31	2.38	1.80
	p to the outer wall, $\lvert j_{p,2+}\rvert$	23.16	23.61	55.46	24.24	18.13
	$s1$ to the outer wall, $\lvert j_{s1,2+}\rvert$	0.62	0.62	29.49	0.24	1.84
	$s2$ to the outer wall, $\lvert j_{s2,2+}\rvert$	0.88	0.75	21.27	0.58	0.24
	$s2$ from the outer wall, $\lvert j_{s2,2-}\rvert$	6.90	7.15	88.47	7.18	4.25
Mean impact energies per elementary particle (eV)	e at the inner wall, $E_{we,1}$	7.92	8.90	12.51	8.18	11.34
	p at the inner wall, $E_{wp,1}$	8.51	9.07	8.51	8.43	11.74
	$s1$ at the inner wall, $E_{ws1,1}$	5.09	3.74	4.13	3.53	3.81
	$s2$ at the inner wall, $E_{ws2,1}$	6.04	8.61	14.13	7.28	8.10
	e at the outer wall, $E_{e,2}$	15.50	15.61	13.89	15.55	11.43
	p at the outer wall, $E_{wp,2}$	16.00	15.99	13.76	15.90	11.86
	$s1$ at the outer wall, $E_{ws1,2}$	5.61	8.06	12.75	5.75	8.14
	$s2$ at the outer wall, $E_{ws2,2}$	9.39	10.15	15.84	4.91	4.07
SEE yields (-)	Non-true-secondaries at the inner wall, $\delta_{NTS,1}$	0.00	0.00	0.58	0.00	0.00
	True-secondary at the inner wall, $\delta_{TS,1}$	0.16	0.17	0.23	0.15	0.21
	Non-true-secondaries at the outer wall, $\delta_{NTS,2}$	0.00	0.00	0.58	0.00	0.00
	True-secondary at the outer wall, $\delta_{TS,2}$	0.28	0.29	0.25	0.29	0.21
Conversion to p and wall collection fractions (%)	$s1$ conversion to p	57.7	58.4	22.5	76.5	52.0
	$s1$ collection at the inner wall	7.1	8.5	3.0	9.5	5.2
	$s1$ collection at the outer wall	35.2	33.1	74.5	14.0	42.8
	$s2$ conversion to p	51.1	55.1	35.4	68.7	52.1
	$s2$ collection at the inner wall	36.2	34.4	40.6	23.2	42.4
	$s2$ collection at the outer wall	12.7	10.5	24.0	8.1	5.5
Replenishment parameter (-)	At the inner wall, $\sigma_{t,1}$	0.04	0.04	0.06	0.04	0.03
	At the outer wall, $\sigma_{t,2}$	0.05	0.04	0.10	0.05	0.03
Electron temperatures at M (eV)	p radial, $T_{rp,M}$	4.86	4.80	4.64	4.81	4.94
	p perpendicular, $T_{\perp p,M}$	7.52	7.58	7.39	7.47	7.78
	$s1$ radial, $T_{rs1,M}$	9.50	8.63	10.81	8.17	9.11
	$s1$ perpendicular, $T_{\perp s1,M}$	2.37	1.85	2.47	1.56	3.02
	$s2$ radial, $T_{rs2,M}$	9.77	9.87	10.37	9.07	9.04
	$s2$ perpendicular, $T_{\perp s2,M}$	4.45	4.59	6.61	3.26	3.02

Table 2: Main parameters characterizing the steady-state discharge for the different cases considered. Time-averaged values over 1 μs of simulation time are considered.

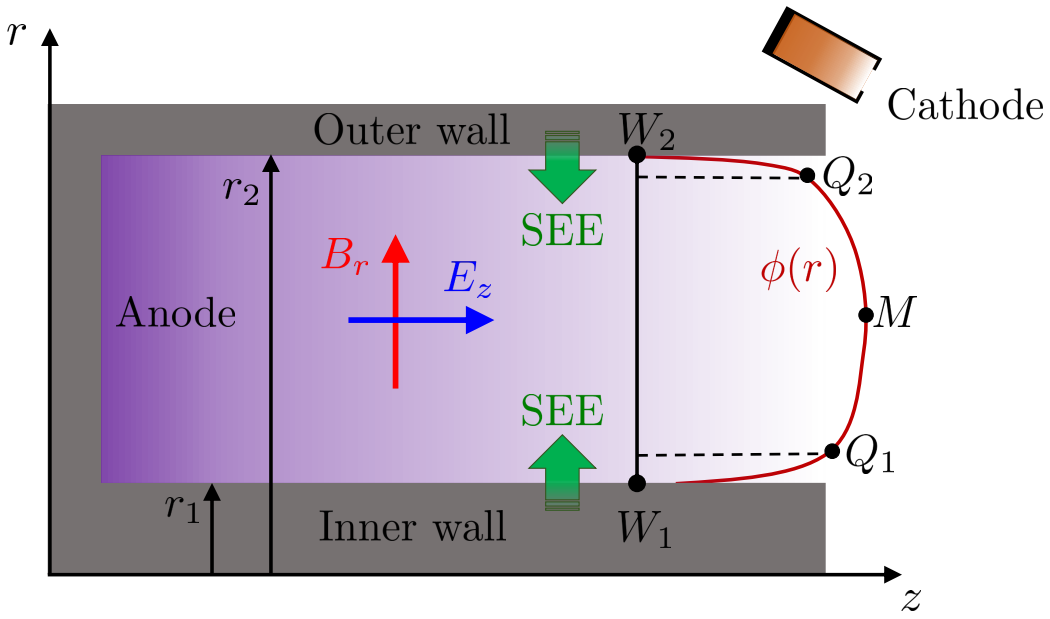

Figure 1: Sketch of a HET. The simulation domain corresponds to the thick black vertical line from the inner to the outer wall. The points W_1, W_2, Q_1, Q_2, and M correspond to the inner and outer walls and sheath edges, and to the channel mid radius, respectively.

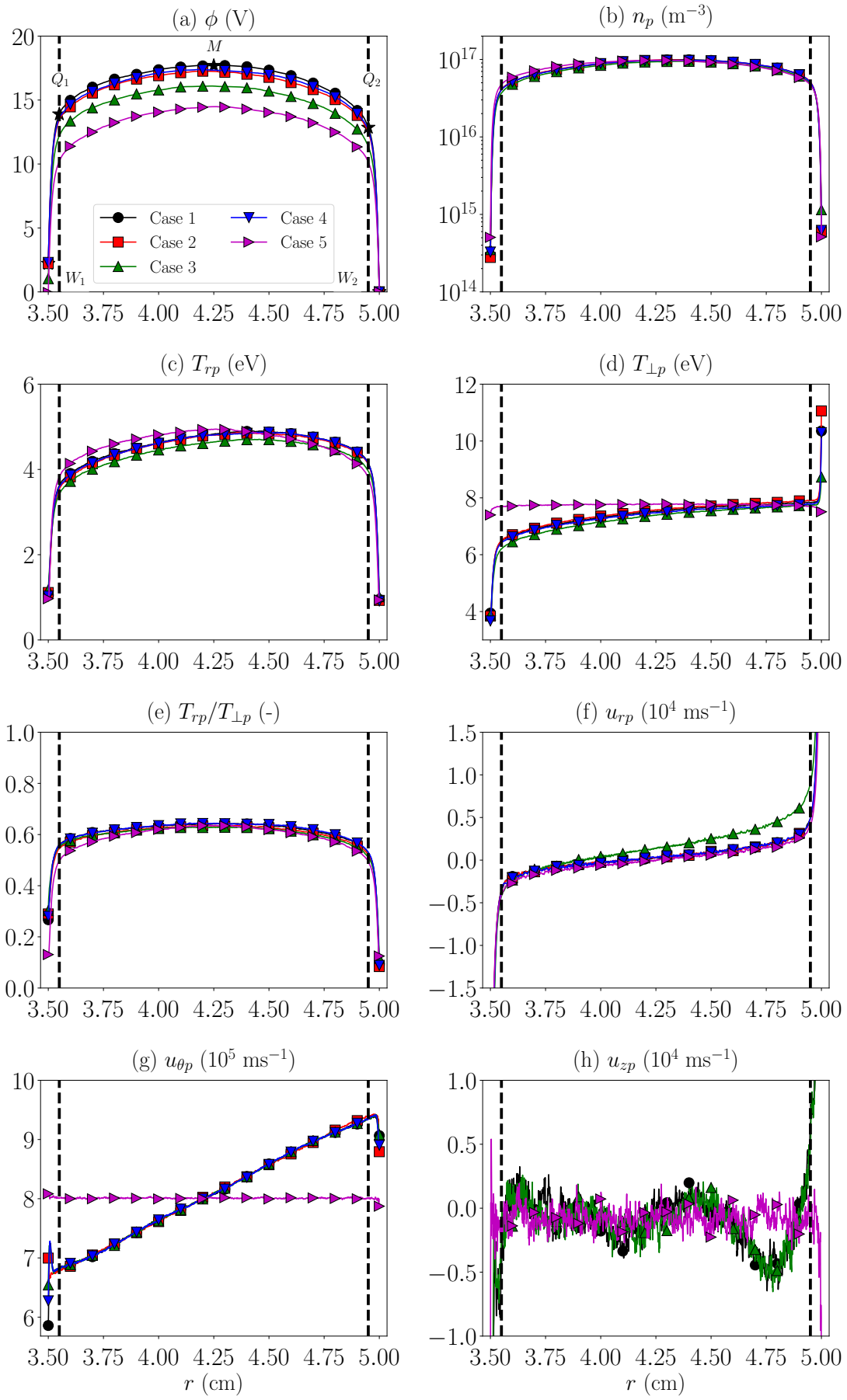

Figure 2: Steady-state radial profiles of different macroscopic magnitudes for primary electrons for cases considered: (a) electric potential; (b) electron density; (c-e) electron parallel (radial) and perpendicular temperatures, and their ratio, respectively; (f-h) radial, azimuthal and axial electron mean velocities, respectively. Black stars on (a) indicates the points at the walls, sheath edges and channel mid radius.

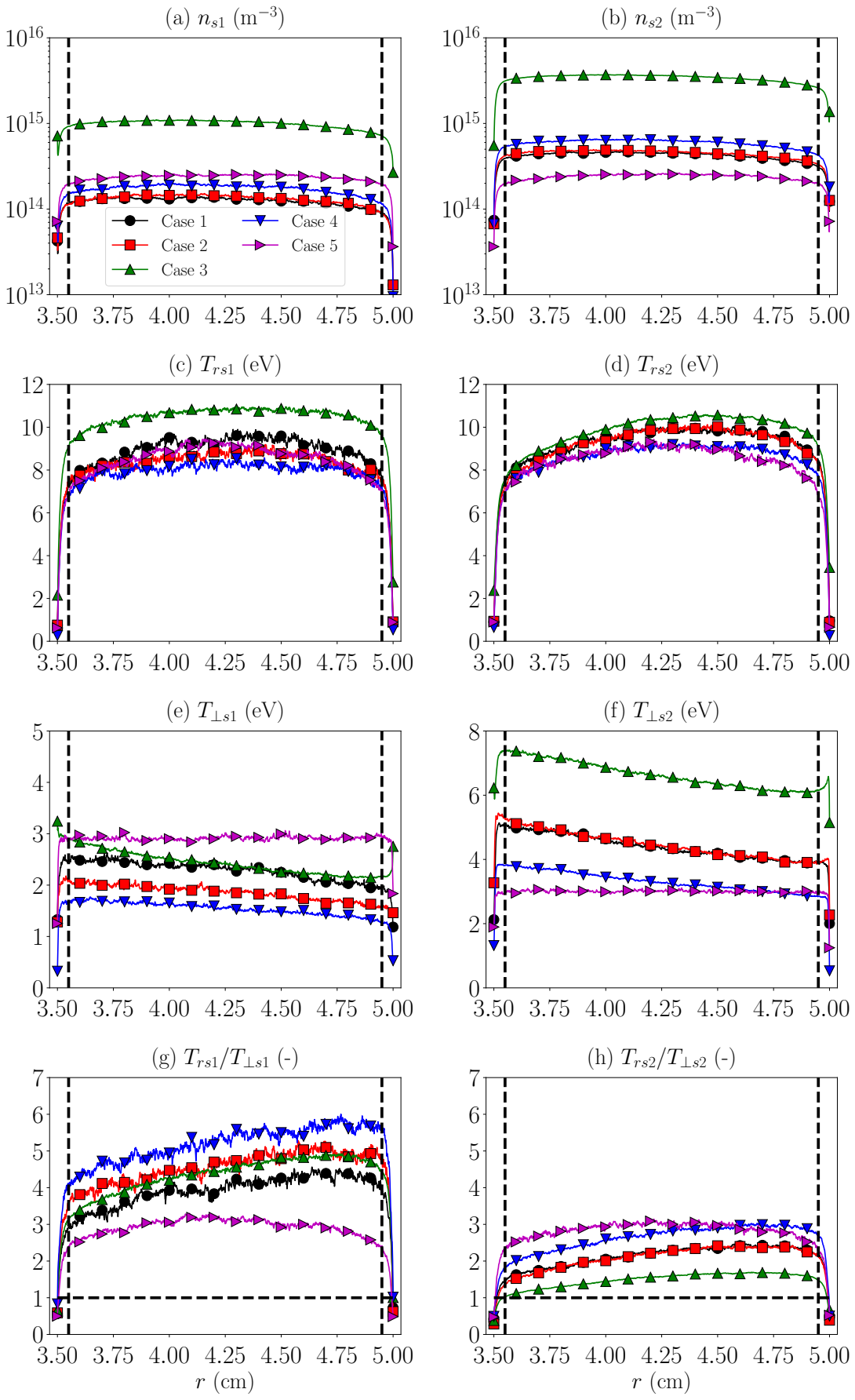

Figure 3: Steady-state radial profiles of different macroscopic magnitudes for secondary electrons for cases considered: (a-b) electron density; (c-d) radial temperature; (e-f) perpendicular temperature; (g-h) temperature ratios, for $s1$ and $s2$ electron populations, respectively.

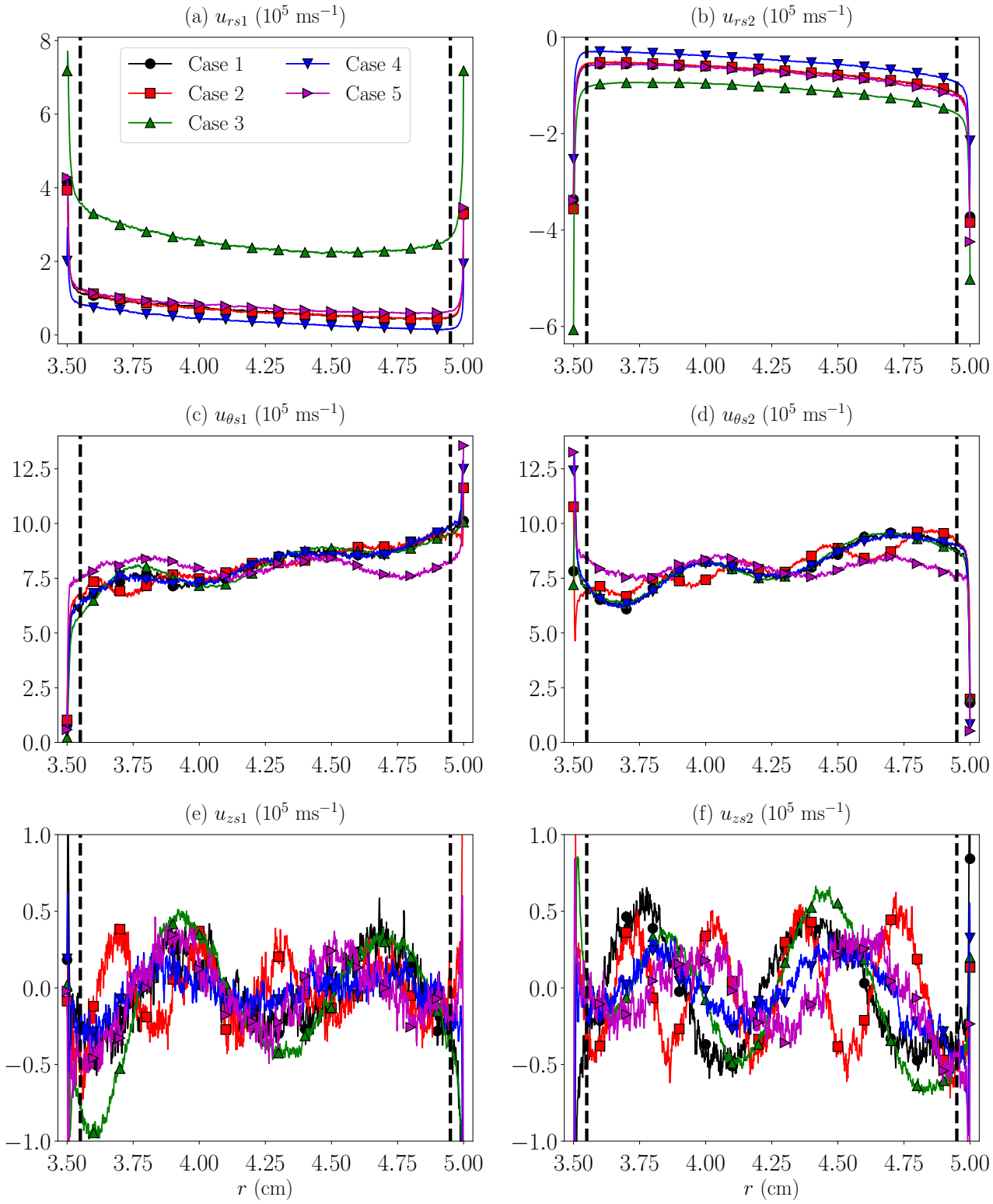

Figure 4: Steady-state radial profiles of macroscopic velocity components for secondary electrons for the cases considered: (a-b) radial velocity; (c-d) azimuthal velocity; (e-f) axial velocity, for $s1$ and $s2$ electron populations, respectively.

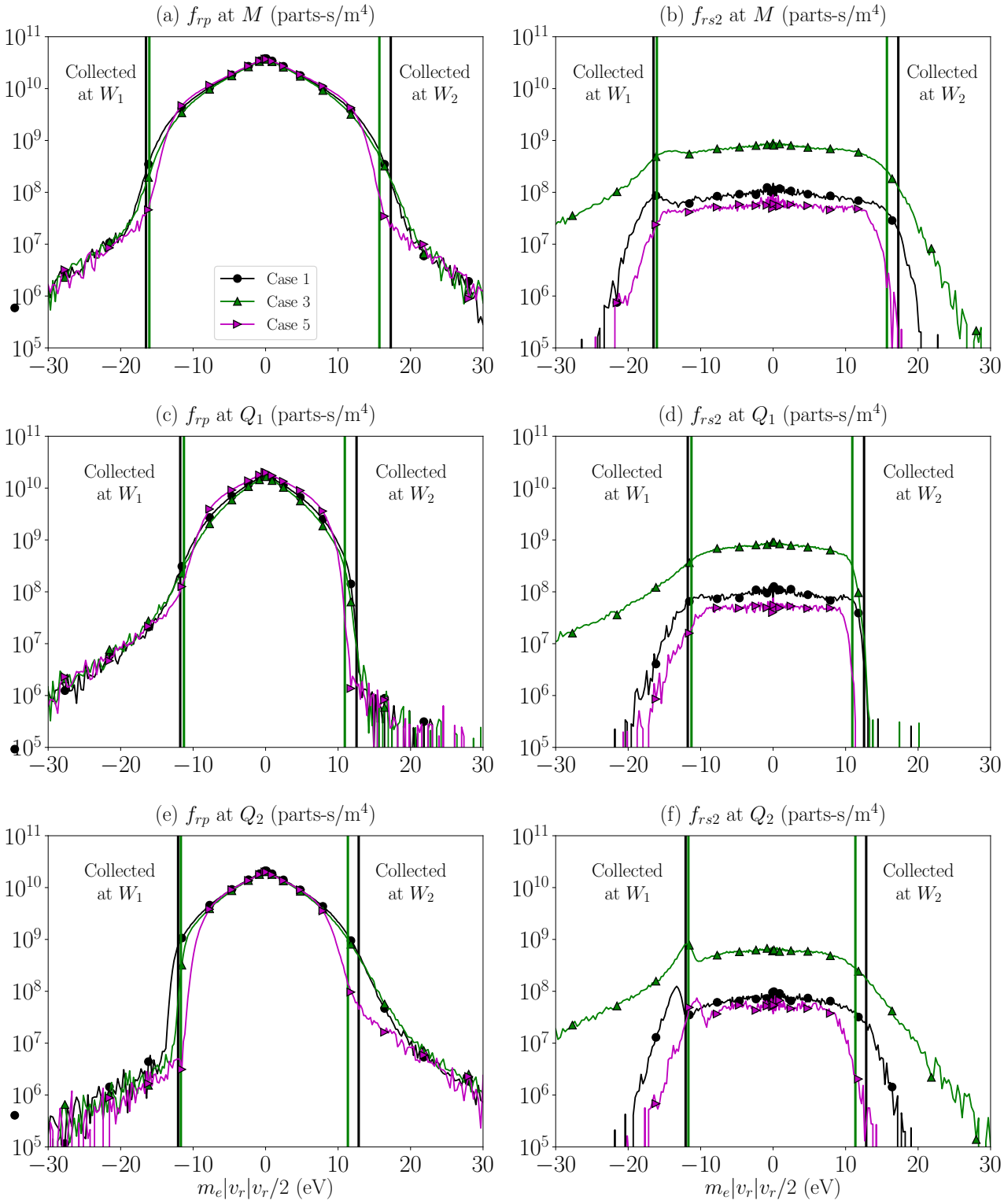

Figure 5: Steady-state radial electron VDFs: (a), (c) and (e) at M, Q_1 and Q_2 for p-electrons, respectively; (b), (d) and (f) at M, Q_1 and Q_2 for $s2$-electrons, respectively. The vertical black and green separate the regions containing radially confined electrons from the inner and outer wall-collectable electrons for Case 1 and 3, respectively. The analogous vertical lines corresponding to Case 5 approximately coincide with those of Case 3 and have been omitted for the sake of clarity.

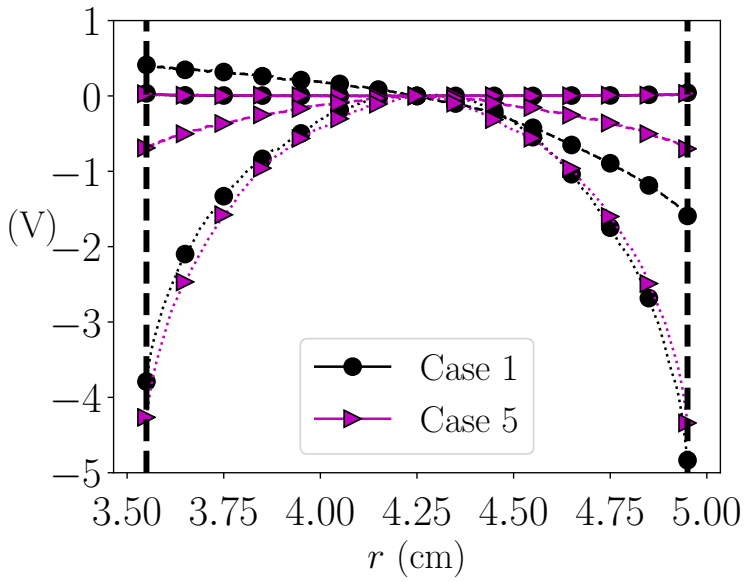

Figure 6: Fulfilment of the integrated radial momentum balance of electrons in Eq. (9) (solid lines); Boltzmann relation (dashed lines); electric potential profile relative to ϕ_M (dotted lines). Dashed vertical lines mark the sheath edges location. The macroscopic variables involved are computed through the EVW algorithm with $N_k = 2 \cdot 10^5$ timesteps (equivalent to 1 μs of simulation time).